Friction anisotropy dependence on morphology of GLAD W films

Guilherme B. Rodrigues*, Nicolas Martin, Fabien Amiot, Guillaume Colas

Université de Franche-Comté, CNRS, SUPMICROTECH-ENSMM, Institut FEMTO-ST, Besançon, 25000, France

Abstract

Scratch tests on tungsten GLAD films examined friction anisotropy at various deposition angles (α), normal forces (F_N), and scratching directions (ϕ). A linear model of the coefficient of friction (μ) revealed four behavior groups, ranging from isotropic ($\alpha = 0°$ and $30°$) to orthotropic ($\alpha \geq 60°$). Intermediate angles ($40° \leq \alpha \leq 60°$) showed slight non-centrosymmetric anisotropy. Post-scratch analysis linked these behaviors to film morphology. A transition from dense to columnar structures, with columns elongated perpendicular to the atom flux, influenced plasticity. Less deformation occurred along scratching directions ($\phi = 90°/270°$) due to column chaining, resulting in higher friction. A mechanical model highlighted how morphology-driven plasticity variations explain the anisotropic behavior.

Keywords: Friction anisotropy, GLAD, Tungsten films, Tilted nanocolumns

1. Introduction

The study of friction is rooted in the first Da Vinci's theories during the 15th century [4]. Since then, following the establishment of a new scientific field called Tribology in 1966 [26], various works have been extensively conducted in order to investigate the complex phenomena that occur when two surfaces come into contact, such as friction anisotropy.

*Corresponding author

Email address: guilherme.bernardes@femto-st.fr (Guilherme B. Rodrigues*)

Friction anisotropy is defined when different coefficients of friction are present depending on the direction or orientation in which two surfaces slide relative to each other [64]. This behavior can be observed due to the crystallography of various materials [14, 23], and it is frequently noticed in biological surfaces and skins of different animals and plants [5, 35, 2]. As a consequence, numerous bio-inspired attempts have been developed using the friction anisotropy such as in surgical graspers and robots climbing slopes [9, 32].

Different techniques of surface texturing have been used to introduce nanostructures on materials surface, leading to friction anisotropy [70, 21]. However, over the last few decades, the advancement of deposition techniques has demonstrated the ability to create columnar structures in thin films. Additionally, by applying an oblique angle, the creation of architectures similar to those observed in nature and produced via surface texturing has been achieved.

The technique which enables the production of these nanostructures is the GLancing Angle Deposition (GLAD) [51]. It is an alternative version of a physical vapor deposition in which the atoms from the target reach the substrate at an oblique angle (α) [20]. By controlling parameters such as substrate temperature, and substrate rotation angles, numerous morphologies can be formed including zigzag structures, helical structures, vertical columns, inclined columns, graded-density structures, s-type structures, and others [20, 52]. Nowadays, given the wide range of possibilities in obtaining nanostructures, GLAD thin films are used in various areas of technology such as optical applications [17, 30], sensors [49], filter and anti-reflection coatings [17], catalysis and biology [44], and solar cells [29, 50].

This micro- and nano-structural organization of films and surfaces has proven to be highly beneficial in achieving anisotropic properties due to their geometric characteristics. These anisotropic behaviors are observed for the electrical properties of GLAD films deposited with different target compositions [12], sputtering pressures, thicknesses [7] and target currents [6]. Furthermore, some studies were carried out to evaluate the anisotropy of thermal conductivity [8] and optical properties [48]. Although the anisotropy of thermoelectrical and optical properties of thin films deposited by GLAD technique have been studied in the last decades, only a few studies have evaluated the mechanical and frictional properties [19, 1, 39]. If literature is focused on friction anisotropy of GLAD films, even fewer studies are found.

Table 1 summarizes studies from 2010 to 2021 on the friction anisotropy

Table 1: Summary of the works studying scratch test on thin films deposited by GLAD technique. SD shortens scratching directions where 0 representing scratching along the columns tilt, 180 against it, and 90/270, perpendicular to it. CP represents the contact pressure and its calculated using the model proposed by [31] and mechanical properties found in [57, 33, 24].

Study	**Material**	**Deposition angle (°)**	**Thickness**	**Indenter tip**	**Normal load**	**SD (°)**	**CP (GPa)**	**Anisotropy?**
[59]	Parylene	35	7.4-22 µm	Spherical diamond tip (17 µm radius)	i) Constant load 100 µN ii) Increasing load 0 - 300 µN	3 directions 0, 90 and 180	0.93	Yes
[22]	Ti	85	39 nm	i) Rectangular flat tip (2 µm x 6 µm) Radii edges = 50 and 75 nm ii) Circular cone (10 µm radius)	0 - 50 µN	2 directions 0 and 180	1.34	Yes
[60]	Cr	0:5:85	850 nm	Si_3N_4 ball (2 mm radius)	10 mN	3 directions 0, 90 and 180	0.22	No
[37]	Mo	0 and 85	not evaluated	90° conical diamond tip (100 µm radius)	100 - 8000 µN	2 directions 0 and 180	2.25	Yes
[36]	Ag	0 and 85	1 µm	90° conical diamond tip (100 µm radius)	100 - 8000 µN	2 directions 0 and 180	0.88	Yes
[42]	Ag	0 and 85	200 nm	Spherical sapphire (400 µm radius)	50 - 700 µN	4 directions 0, 90, 180 and 270	0.23	Yes

of GLAD films subjected to scratching tests [59, 22, 60, 37, 36, 42]. Due to variations in film materials, thicknesses, and tribological conditions, direct comparisons of the GLAD films' behavior are difficult. However, most studies consistently observed anisotropy between scratching along (0°) and against (180°) the column tilt.

Three studies also evaluated the perpendicular directions (90° and 270°) to investigate whether, in addition to a non-centrosymmetric anisotropy, another type of anisotropy could be detected. One study found no anisotropy in any of the three directions (0°, 90°, and 180°) [60], saying it was due to the indenter (a 2 mm radius Si_3N_4 ball) not being sensitive to the column orientation. Another study found smaller friction coefficients at 180° compared to 0° and 90° [59], but it used different test conditions and data processing. Finally, [42] tested four directions and found that only one-arm films had higher friction coefficients at 90° and 270°, especially at lower normal loads.

The anisotropic behavior observed between 0° and 180° is commonly explained by different deformation modes of the columns when scratching along and against their tilt [22, 37, 36, 42]. This is usually studied by examining a single column's behavior, either through finite element analysis [22] or a force balance system [59, 36, 42]. However, this approach may overlook the fact that the indenter slides over a "forest" of columns, not just one [22]. Additionally, several studies have linked anisotropic behavior to the columns' morphology [13, 11, 34, 43], which is often neglected as a factor. Overall, there is a lack of comprehensive analysis on this topic, which could provide insights into the presence of plastic deformation and how it behaves in different scratching directions.

Additionally, as shown in Table 1, the authors limited their scratching directions to two, three or four orientations. Considering that most GLAD films have complex three-dimensional geometries and microstructures, limiting the evaluation to a few directions can overlook the possibility of determining different behaviors along other directions, as it was already reported for magnetic, optical and friction properties [15, 65]. This emphasizes the need to evaluate the friction anisotropy of GLAD films more thoroughly.

GLAD enables the deposition of a wide range of materials, such as metals, as well as oxides, ceramics and polymers. Among these materials, tungsten has been extensively studied due to its combination of excellent mechanical properties, high thermal stability, and high electrical conductivity [6]. Additionally, tungsten is utilized in various thin film technologies, such as diffusion barriers [53], X-ray filters [47], and field emitters [69]. Additionally, tungsten has demonstrated flexibility in parameterization for the development of nanostructures [12], making it the material of focus in this study.

In this context, the present study aims at evaluating the presence of friction anisotropy in tilted columnar tungsten films deposited using the GLAD technique. To investigate this, a series of films were deposited at various angles (α) from 0° to 85°, and their morphology and crystallography were analysed. Subsequently, scratch tests were conducted with varying normal forces (F_N) at four levels and scratching directions (ϕ) at eight angles to obtain coefficient of friction data. This data was processed using a linear mathematical model to fit experimental results and to determine an anisotropy degree, enabling quick identification and quantification of friction anisotropy, as well as its type, symmetry aspects and form. All these analyses are conducted with a detailed uncertainty traceability, ensuring a 95 % confidence level in all results. Sequentially, post-scratching examinations of the films

provide insights into the correlation between friction results, anisotropy, and the films morphology and crystallography. These observations suggest that the friction anisotropy results from plasticity, which is driven by the morphology. A mechanical model is proposed to analytically show this potential influence of plasticity on friction behavior.

2. Materials and Method

Tungsten thin films were deposited on 20 × 10 mm^2 Si(100) substrates of 525 µm thickness using a homemade GLAD system. A 99.9 % purity target of 20 cm^2 was positioned 60 mm away from the substrate in a chamber which was pumped down until reaching a residual vacuum of about 10^{-5} Pa. During the deposition, neither rotation nor heating of substrate was applied, and the current in the target was set at 140 mA. In order to evaluate the influence of the deposition angle (α), depositions were performed at $\alpha = 0°$, 30°, 40°, 50°, 60°, 70°, 80°, and 85°. Argon flow rate was kept at 2.6 sccm with a corresponding sputtering pressure of about 2.8 × 10^{-1} Pa. The deposition time was adjusted to obtain film thicknesses in the range of 520 ± 50 nm for all α.

Top and cross-sectional views of cleaved samples were captured using a ThermoFisher Apreo S low-vacuum scanning electron microscope (SEM) to characterize the film morphology. Thickness (t) of each film was measured using a Brucker Profilometer model DEKTAK XT. A 12.5 µm radius tip with a 45° cone angle was used to apply a normal force of 0.06 mN over a 800 µm scan length. Nine measurements were distributed in both extremities and the center of the samples in order to verify the thickness variation along the samples length. These thicknesses were checked from the cross-section views which were also used to determine the angle of inclination (β) of the films columnar microstructure. For β values, ten measurements along different cross-section regions were performed (Fig. 1(a)), averaged and presented with one standard deviation.

Regarding the crystallography, grazing X-ray diffraction (GIXRD) scans were performed on a Malvern Panalytical Aeris diffractometer (Cu K-α radiation = 1.5418 Å) working at 30 kV and 10 mA, and setting a grazing incidence angle of 0.8°. The scans were performed with the diffraction angle varying from 20° to 90°.

2.1. Scratching tests

Scratching tests were performed using an Anton Paar GmbH Micro Scratch MST and a spheroconical Rockwell diamond tip indenter (100 µm radius and conic angle of 120°). The tests were conducted at room conditions with the relative humidity being 47 ± 2 % and the temperature in the range of 22 ± 0.6 °C. A constant normal force was applied in a 0.5 mm scratch length with a sliding speed of 6 mm/min. This velocity was selected based on preliminary tests, which demonstrated that this variable has no influence on the friction response of the films (cf. Section 1 of supplementary information). The normal and tangential forces (F_N and F_T, respectively) were measured with a 6 mN resolution, and Coulomb's law was applied to calculate each F_T/F_N experimental point. Four different values of F_N were applied: 1.50 N, 2.50 N, 3.25 N and 4.00 N, which corresponds to contact pressures, estimated using the model proposed by [31], between 7 and 18 GPa, depending on α. These contact pressures are considerably larger than those applied in literature (Table 1). Furthermore, these loading levels were chosen after carrying out preliminary test using increasing load scratch tests (from 0.1 N to 8.0 N) on 2 mm length scratches and evaluating at which loads the tangential force measurement was statistically reliable and from which loads the film degradation started.

For the above mentioned deposition parameters and without any rotation of the substrate, the films generally exhibit an inclination facing the incoming tungsten atoms, Fig. 1(a). This asymmetry results in the greater focus on verifying the anisotropy between 0° and 180°, as previously shown in Table 1. However, in this work, a detailed mapping of frictional behavior is evaluated by defining eight different scratching directions (ϕ). These directions were specified based on the tungsten atom flux for a non-normal deposition ($\alpha \neq 0°$). When the indenter moves along the same direction than the film inclination, the scratching direction is defined as $\phi = 0°$. Similarly, if this movement is the opposite, $\phi = 180°$. Finally, the eight directions can thus be defined by rotating counterclockwise (Fig. 1(b)). Three repetitions were conducted for each condition, and for each repetition, the average μ was calculated based on the stable portion of the F_T/F_N *versus* displacement curves. The data characterized by the presence of the static coefficient of friction (μ_s) as the indenter starts to probe the samples, was eliminated of the average calculation, as shown in Fig. 1(c).

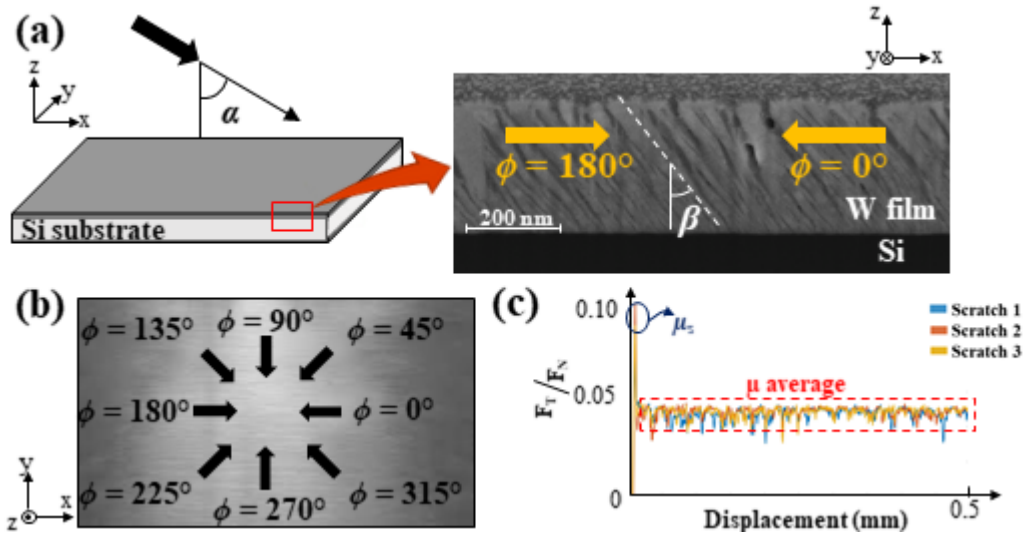

Figure 1: (a) A schematic representation shows the deposition angle, α, which implies in a directional columnar growth pointing towards the tungsten atom flux. This tilt is used to determine the scratching direction at $\phi = 0^{\circ}$, scratching along the columns tilt, and $\phi = 180^{\circ}$, scratching against it. (b) By rotating counterclockwise in steps of 45°, all eight ϕ directions are defined. (c) Finally, for each ϕ, the average for coefficient of friction, μ, is calculated using the stable portion of F_T/F_N *versus* displacement curves.

2.2. Friction anisotropy

In order to describe the frictional anisotropy, one makes use of the anisotropic extension of Coulomb's law in a sole sliding regime proposed by [73, 74]. Therefore, the friction force $\underline{F}_f$ belongs to $\mathbb{R}^2$ and it can be described by Eq.(1) as a function of the normal force and the sliding direction, $\underline{v}$.

$$\underline{F}_f = -|\underline{F}_N| \cdot f(\underline{v}) \tag{1}$$

$$\underline{v} = \begin{bmatrix} \cos(\phi) \\ \sin(\phi) \end{bmatrix} \tag{2}$$

One assumes for ϕ a linear function of $\underline{v}$ following $f(\underline{v}) = \mathcal{C} \cdot \underline{v}$, where $\mathcal{C}$ is a second-order tensor of $\mathbb{R}^2$ and may be decomposed as $\mathcal{C} = \tilde{\mathcal{C}} + \mathcal{A}$, where $\tilde{\mathcal{C}}$ is the symmetric part and $\mathcal{A}$ is the anti-symmetric one. Here, contrary to the set-ups in [46, 18], using a scratch tester, the sole projection of $\underline{F}_f$ along $\underline{v}$ is measured. As a consequence, only the symmetric part of $\mathcal{C}$ is assessed:

$\underline{v} \cdot \mathcal{C} \cdot \underline{v} = \underline{v} \cdot \tilde{\mathcal{C}} \cdot \underline{v} + 0$. $\tilde{\mathcal{C}}$ may be conventionally described by its singular value decomposition (SVD):

$$\begin{bmatrix} C_{11} & C_{12} \\ C_{12} & C_{22} \end{bmatrix} = \tilde{\mathcal{C}} = \mathcal{U} \cdot \mathcal{G} \cdot \mathcal{U}^t = \begin{bmatrix} \cos(\gamma) & -\sin\gamma \\ \sin\gamma & \cos(\gamma) \end{bmatrix} \begin{bmatrix} g_1 & 0 \\ 0 & g_2 \end{bmatrix} \begin{bmatrix} \cos(\gamma) & -\sin\gamma \\ \sin\gamma & \cos(\gamma) \end{bmatrix}^t \tag{3}$$

The angle γ represents the inclination of the principal direction of the fitting curve in relation to scratching direction. The matrix $\mathcal{G}$ is diagonal and its diagonal terms g_i are positive. They define the coefficients of friction along the principal directions of the fitting curve, as it can be seen in Fig. 2.

Using this linear model, one imposes that the friction anisotropy is centrosymmetric and is described through 3 parameters (C_{11}, C_{12}, C_{11}) or (γ, g_1, g_2). Using the components of $\tilde{\mathcal{C}}$, the coefficient of friction $\mu(\phi)$ is

$$\mu(\phi) = C_{11}\cos^2\phi + 2C_{12}\cos\phi\sin\phi + C_{22}\sin^2\phi \tag{4}$$

Considering the eight scratching direction measurements ϕ_i, the equation above is recast as a linear system

$$\mathcal{M} \cdot \underline{C} = \underline{\mu} \tag{5}$$

where $\underline{\mu} = [\mu(\phi_1), ..., \mu(\phi_8)]^t$, $\underline{C} = [C_{11}, C_{12}, C_{22}]^t$. $\mathcal{M}$ is the matrix such that $\mathcal{M}_{i1} = \cos^2\phi_i$, $\mathcal{M}_{i2} = 2\cos\phi_i\sin\phi_i$ and $\mathcal{M}_{i3} = \sin^2\phi_i$. This system is over-determined and is thus solved in a least-square sense to provide the sought parameters

$$\underline{C}_{lsq} = (\mathcal{M}^t \cdot \mathcal{M})^{-1}(\mathcal{M}^t \cdot \underline{\mu}) \tag{6}$$

The difference between linear model fit and experimental points is assessed using $\underline{R} = \mathcal{M} \cdot \underline{C}_{lsq} - \underline{\mu}$, which is applied to calculate the global residual $\eta = \sqrt{\frac{\underline{R}^t\underline{R}}{\underline{\mu}^t\underline{\mu}}}$.

The parameters γ, g_1 and g_2 are then obtained and a normalized anisotropy degree is then defined as $\overline{\Delta g} = 2(g_1 - g_2)/(g_1 + g_2)$. An isotropic case corresponds to $g_1 = g_2$ and $\overline{\Delta g} = 0$. A propagation of the uncertainties during all force measurements and calculations was performed in order to guarantee a confidence level of 95% for the results (cf. Section 2 of supplementary information).

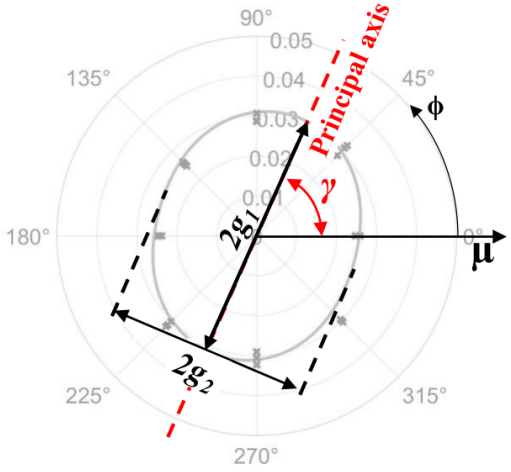

Figure 2: Example of a polar plot and the fitting curves for the coefficient of friction (μ) data of all eight scratching directions evaluated (ϕ). The linear model used to perform this fit provides the parameters γ, which represents the inclination of the fitting curve, and g_1 and g_2, which are the diagonal terms, defining the friction coefficients along the principal directions.

2.3. Post-scratch investigations

Post-scratch investigations were conducted by performing Focused Ion Beam (FIB) cross-sections, using a Zeiss Ultra 55 MEG-FEG FIB. A protective platinum layer was deposited before etching the surface, followed by a cross-section cleaning procedure. The cross-sections were then observed using Scanning Electron Microscopy (SEM). To ensure consistency in the analysis, FIB zones were positioned in close proximity and in regions with similar thickness, accounting for potential variations in film thickness. Additionally, SEM images of the films surface, both in as-deposited conditions and after scratch tests, were acquired using a Thermofisher Apreo S in low-vacuum mode.

3. Results and Discussion

3.1. As-deposited W films

All films thickness averages lie in the range 520 $\pm$ 50 nm and the columns are tilted at various β angles pointing towards the atom flux, as listed in

Table 2. Column inclination is a well-known characteristic of GLAD films, with β consistently smaller than α [20]. In the W GLAD films studied herein, for the film deposited at $\alpha = 0°$, the columns are perpendicular to the substrate, as expected. As α becomes higher, β increases in a non-linear relationship, which is consistent with the literature [20]. Numerous empirical models have been used to predict β [38, 63]. However, it has been shown that β is material-dependent [72] and influenced by several deposition parameters [12, 43, 45]. As such, none of these models can be directly applied to the β results obtained in this study.

Table 2: Summary of tungsten films deposited by GLAD at various deposition angles.

Deposition angle, α (°)	Deposition time	Thickness (nm)	Growth rate (nm/h)	Column angle, β (°)
0	29'45"	553 ± 10	1115 ± 20	0.1 ± 2.8
30	32'53"	530 ± 20	965 ± 36	8.4 ± 1.3
40	41'48"	525 ± 30	753 ± 43	13.5 ± 2.9
50	39'40"	538 ± 43	812 ± 65	17.3 ± 3.0
60	36'39"	510 ± 50	832 ± 82	24.1 ± 3.7
70	42'19"	540 ± 39	766 ± 55	30.7 ± 3.0
80	82'27"	570 ± 38	414 ± 28	37.3 ± 1.1
85	104'24"	545 ± 25	313 ± 14	36.5 ± 1.3

Figure 3 shows surface and cross-section views of W films deposited at $\alpha = 0°$, 50°, 70° and 85°, with the yellow arrow indicating the atom flux direction (cf. Section 3 of supplementary information for all films). Although the films deposited at $0° \leq \alpha \leq 40°$ present a columnar formation, which can be seen for the film deposited at $\alpha = 0°$, they are dense and compact (Figs. 3(a) and (b)). The columns are close to each other, characterizing a fibrous feature. These morphology changes when α reaches 50°, as larger columns and voids separating some of them are observed. It means that the porosity of the films starts to increase with appearance of open porosities, even though it remains dense and compact at $\alpha = 50°$, as shown in Fig. 3(c).

Columnar formation continues to evolve for larger α angles, as shown in Figures 3(e)-(h). From $\alpha \geq 60°$, a well defined columnar structure with larger columns, more widely spaced and with an increased porosity, is evidenced by the presence of voids between the columns. Most importantly, the top views of these films show columns that are more elongated in the direction perpendicular to the arrival of W atoms, corresponding to $\phi = 90°/270°$.

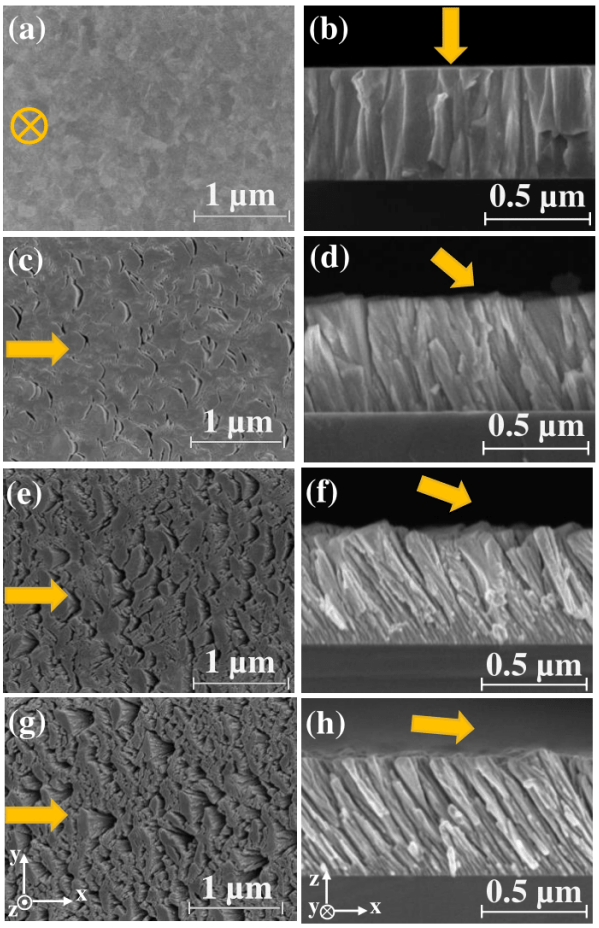

Figure 3: Surface and cross-section views by SEM of tungsten films obtained by GLAD deposition performed at various deposition angles. (a)-(b) $\alpha = 0°$, (c)-(d) $\alpha = 50°$, (e)-(f) $\alpha = 70°$ and (g)-(h) $\alpha = 85°$. The yellow arrows indicate the direction of the tungsten atom flux during deposition.

Morphologies observed herein are consistent with those reported from W, W-Cu and W-Ag films [6, 12, 7, 8, 13, 45]. These studies explain the strong influence of the shadowing effect on the micro- and nano-structure of the films when $\alpha > 60°$, identified as a critical angle [56]. At these deposition angles, atoms are initially randomly distributed on the substrate and, as the growth continues, some structures start to nucleate. These structures evolve into column features fanned out along the perpendicular direction to the flux

of atoms [20]. This phenomenon is directly related to the diffusion energy of the W atoms. As the columns grow, the shadowing effect intensifies, preventing the W atoms from reaching the shadowed regions. Consequently, well-defined columns with more voids between them and elongated in the normal direction to the atom flux are formed. Similar morphologies have been reported in literature [66, 58, 38]. When $\alpha < 60°$, the shadowing effect is less significant and does not greatly influence the morphology, because the angle is not high enough to generate extensive shadowed regions. Therefore, W atoms arrive with a more uniform distribution [66, 20], which explains the morphological characteristics of films deposited at $0° \leq \alpha \leq 50°$.

X-ray diffractograms of W films are presented in Figure 4. Several planes of body centered cubic, bcc-W and A15-W phases are identified. The (110) and (211) planes of bcc-W phase represent the highest diffracted peaks (2θ = 40.2° and 73.1°, respectively), and their intensity are larger for the films deposited at 40° and 50°. This bcc-W phase formation during magnetron sputtering have been already reported in many studies [68, 40, 41, 28]. On the other hand, A15-W phase is well known for presenting higher electrical resistivity [41] and hardness [62]. However, its growth process, composition and structure are still discussed in literature. It has been proposed that it is a form of tungsten oxide [16], while another part of scientific community stands that this phase is stabilized by impurities, such as oxygen, but without formation of oxide [40, 41].

Similarly to what is done by [71, 61], in order to evaluate the presence of A15-W phase, the ratios of A15-W peak intensities in relation to the bcc-W planes are evaluated in the Table 3. Different ratios of the sum of A15-W peak intensities (I_{A15-W}), to the intensities for each (110), $I_{(110)}$, and (211), $I_{(211)}$, planes of bcc-W are observed. Similarly to what was previously observed for the morphology, two groups may be defined herein: i) $0° \leq \alpha \leq 50°$ and ii) $60° \leq \alpha \leq 85°$. The first group exhibits lower ratios indicating that in proportion the quantity of A15-W phase identified in the XRD analyses is not significantly important when compared to the second group. As α reaches 60°, the presence of A15-W phase increases substantially, getting to a maximum for the film deposited at $\alpha = 85°$.

The bcc-W phase is the most thermodynamically stable and the surface adatom mobility is considerably higher in comparison to the A15-W phase [40, 55, 68]. When a GLAD deposition is performed at α closer to 0°, the adatom mobility remains and the bcc-W phase islands grow faster, covering up the A15-W islands [27].

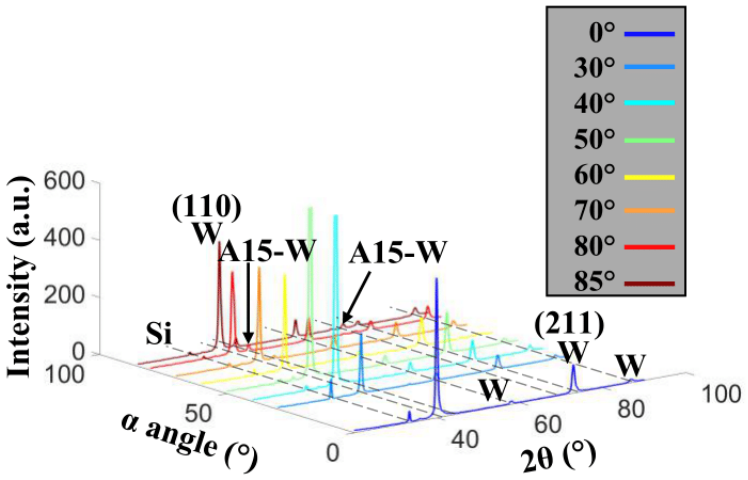

Figure 4: XRD patterns of tungsten films deposited at various deposition angles. Silicon, α-W phase and β-W meta-stable phase are identified.

Table 3: Ratios of A15-W intensities to bcc-W planes (110), $I_{A15-W}/I_{(110)}$, and (211), $I_{A15-W}/I_{(211)}$ obtained from the XRD patterns

Deposition angle, α (°)	$I_{A15-W}/I_{(110)}$ (x10^{-3})	$I_{A15-W}/I_{(211)}$ (x10^{-2})
0	28	13
30	54	20
40	13	17
50	12	9
60	102	33
70	80	36
80	150	119
85	201	327

However, as α increases the shadowing effect becomes more important, resulting in higher surface diffusion from bcc-W to lower adatom surface islands (A15-W). This enables a favorable growth of A15-W phase in the first stages of growing process, and consequently, it is expected that A15-W islands are more concentrated close to the substrate [3].

Although the A15-W phase nuclei become more important for higher α, this phase is considerably unstable and may transform into bcc-W phase [68, 55]. This stability of A15-W phase is significantly influenced by the oxygen presence [55, 68]. As conditions applied during all depositions are relatively the same, the amount of A15-W phase is attributed to the increase of α. A higher volume of voids allows more interaction between A15-W phase and oxygen [25, 67]. Additionally, at lower deposition rates, the residual oxygen in the chamber has more time to be incorporated during the deposition, increasing the probability of A15-W phase nucleation [54]. As higher α implies in lower deposition rate (Table 2) [20] and in a more porous microstructure (Fig. 5), more formation and stabilization of the A15-W phase are observed.

3.2. Friction behavior

A detailed analysis was conducted, comparing results for four F_N values (1.50 N, 2.50 N, 3.25 N and 4.00 N) for each α and in all ϕ directions. The uncertainties associated with measurement and calculation of the coefficient of friction (μ) were considered. No significant statistical differences were found between the values, indicating that, at a 95 % confidence level, the μ for all ϕ directions does not depend on the applied normal force, providing a verification of Coulomb's friction law in the chosen range of tribological conditions (cf. Section 4 of supplementary information). Therefore, in the following, only data for $F_N = 3.25$ N are presented, plotted in polar plots, and fitted with the linear model. This choice was made because smaller normal forces exhibit larger measurement dispersion, and although optical analyses have not confirmed any degradation, the normal load of 4.00 N sometimes approaches to the critical load values identified in preliminary increasing load tests.

Figure 5 shows the $\mu(\phi)$ in polar form for the scratching tests performed with $F_N = 3.25$ N on the films deposited at α ranging from 0° to 85°. Symbols represent all the experimental points of μ for each scratch performed at each ϕ, while the solid line is the fit of the data points by the linear model application. Dotted lines represent the statistical interval of coefficient of friction values for the fit with a 95 % confidence level. Based-on the curves shape, symmetry aspects, $\overline{\Delta g}$ (Fig. 6) values, and residuals (Fig. 7), four groups of films can be distinguished (cf. Section 5 of supplementary information for the definition of the applied terms, such as orthotropy and non-centrosymmetric).

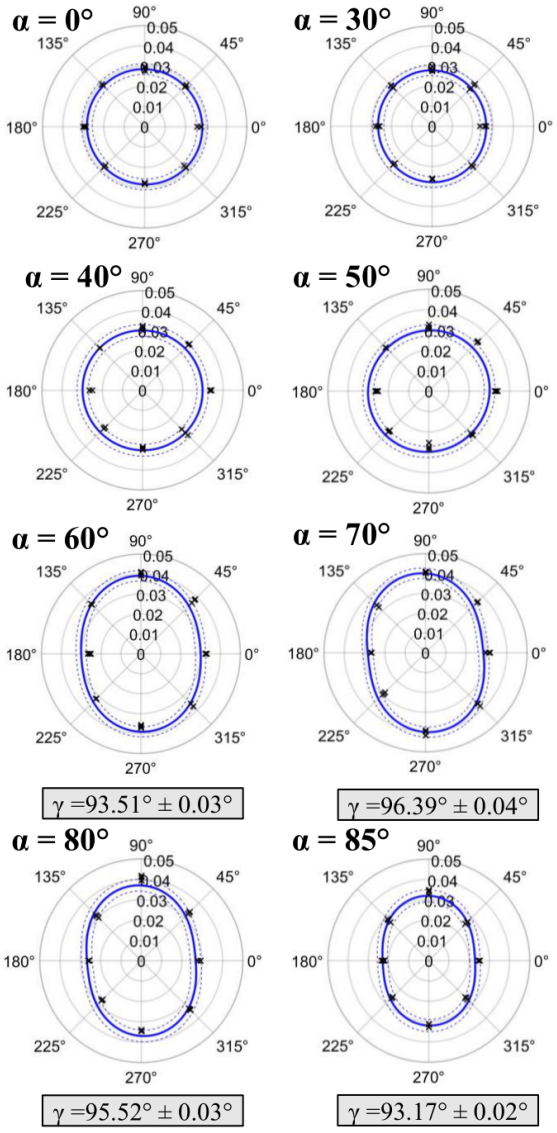

Figure 5: Coefficient of friction, μ, as a function of scratching directions, ϕ, for the eight deposition angles, α. The symbols represent the experimental points of μ. The solid line is the fit of the data points obtained by the linear model, and the dotted lines represent the statistical interval for the fit values with a confidence level of 95 %. Additionally, the inclination of the fitting curves, γ, is presented for the second group of films ($60^{\circ} \leq \alpha \leq 85^{\circ}$).

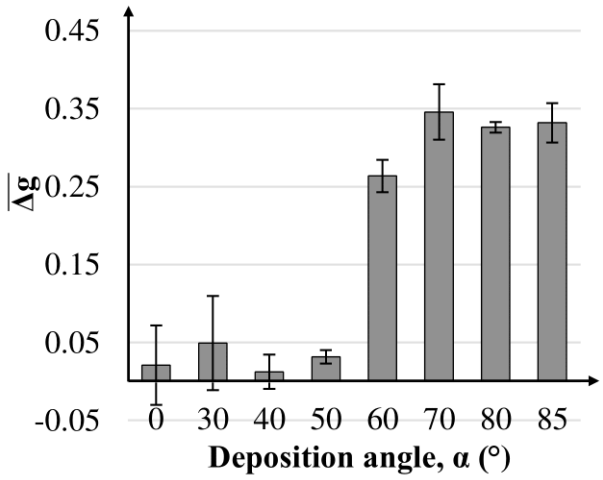

Figure 6: Anisotropy degree, $\overline{\Delta g}$, obtained using the linear model for all deposition angles, α.

1. $\alpha = 0°$ and 30°: Isotropic behavior confirmed by circular shaped curves, lower residuals and nearly null $\overline{\Delta g}$ values. The error bars are significantly larger than the average, even extending into negative values for $\overline{\Delta g}$. However, since $\overline{\Delta g}$ cannot be negative, these results suggest that the statistical value of $\overline{\Delta g}$ is close to zero for both films, and greater uncertainty in the post-treatment of these fitting curves is observed.
2. $\alpha = 40°$ and 50°: Although, they present circular shaped curves and low $\overline{\Delta g}$ values, a subtle shift in relation to the symbols can be observed, mainly due to a slight non-centrosymmetric anisotropy between $\phi = 0°$ and 180°. As the applied linear model imposes a centro-symmetric curve, this anisotropy results in the observed offset in these two directions. Some of the symbols are out of the dotted-line interval, indicating that they are statistically different. This difference is confirmed by the increase of the global residual η.
3. $\alpha = 60°$: Elliptical-shaped curve and larger $\overline{\Delta g}$ value are noticed, characterizing the presence of an orthotropy where considerably larger μ are observed when scratching at $\phi = 90°$ and 270° than the other scratching directions. Additionally, a subtle offset in relation to experimental data is observed, due to a slight difference between scratching at $\phi = 0°$ and $\phi = 180°$, resulting in a global residual in the same order of those

obtained for $\alpha = 40°$ and $50°$.

4. $70° \leq \alpha \leq 85°$: Elliptical-shaped curves are observed. The films deposited at $\alpha = 70°$ and $80°$ exhibit larger residuals, indicating a slight non-centrosymmetry. However, this non-centrosymmetry remains within the same order of magnitude of the uncertainties. This is confirmed by the fact that the experimental points remain within the dotted-line interval. As α increased further, the non-centrosymmetric behavior becomes even less pronounced, as observed for $\alpha = 85°$. This confirms that these films present only an orthotropic behavior, as indicated by the larger $\overline{\Delta g}$ values, which are approximately 0.35 for all three films.

For groups 3 ($\alpha = 60°$) and 4 ($70° \leq \alpha \leq 85°$), the orthotropy shows larger coefficient of friction for $\phi = 90°$ and $270°$, which align with the direction perpendicular to the atom flux. This behavior is confirmed by the γ values obtained, which are close to $90°$.

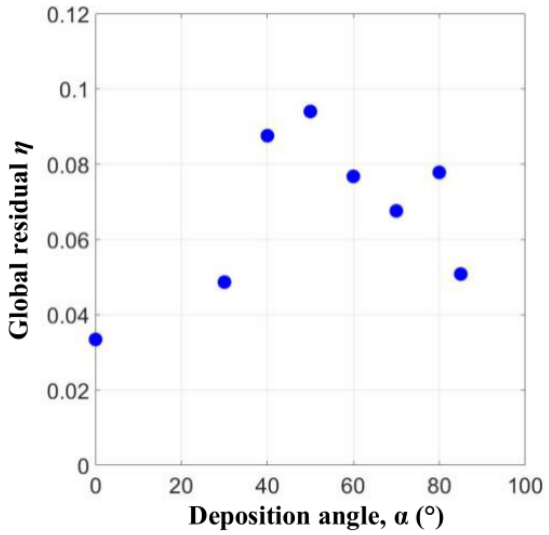

Figure 7: Global residual η of the linear model for the $\mu(\phi)$ curves of all tungsten films deposited at different deposition angles (α) and scratched at different normal loads (F_N).

The literature suggests that friction anisotropy in GLAD films is primarily attributed to the tilt of the columns and the resulting asymmetry between $\phi = 0°$ and $\phi = 180°$ [59, 22, 37, 36, 42]. However, the results observed in

this study indicate that while this anisotropy exists, as seen for groups 2 (α = 40° and 50°) and 3 (α = 60°), it might be influenced by other factors. The primary friction anisotropy governing the W films in this study, under the contact conditions applied, exhibits an orthotropic character (i.e., ϕ = 90° and 270° *vs.* other directions) for $\alpha \geq 60°$, which is far more prominent than the subtle non-centrosymmetric anisotropy between ϕ = 0° and 180°.

3.3. Post-scratching morphological aspects

Figure 8 compares SEM images from surface views of as-deposited zone and scratched zones for films deposited at α = 50° and 80°. No significant difference between the as-deposited zone and scratched zone is observed for the film deposited at α = 50°. However, the one obtained at α = 80° shows an important variation, indicated by the compaction of the film and smashing of the column apex.

Similar observations can be done on Figure 9 where FIB cross-section views of the same films deposited at α = 50° and 80° are shown. An as-deposited zone and three scratched regions, ϕ = 0°, 90° and 180°, are observed. For α = 50°, as for the surface views, there is no significant difference between the film before and after scratching. Its compactness is confirmed, as the columns indeed touch each other and form an almost continuous "wall". However, the topography formed by the tops of the as-deposited columns disappears after scratching, as after being loaded they appear to present the same height, resulting in a flatter and more uniform top surface. It is also evident that regardless of the scratching direction, the columns deform very little, which is indicated by the small difference in thickness before and after scratching. This primarily deformed region is similar for the three ϕ observed. Given that the film is compact, with a few voids between the columns, the indenter deforms the columns tips when sliding over them, but there is no room for deformation in other directions. This behavior aligns with the circular shape of the friction coefficient curve of the film, reflecting similar friction coefficients in all directions. However, it does not fully account for the slight non-centrosymmetric behavior observed.

For the film deposited at α = 80°, the columns deform considerably more than the one deposited at α = 50° (Fig. 8), as clearly shown by the reduction in film thickness after scratching (Fig. 9). Globally, the column tips undergo large plastic deformations without fracturing in all three scratching directions, resulting in a smooth, flatten top surface. However, unlike the film deposited at α = 50°, there is a significant deformation at the level of

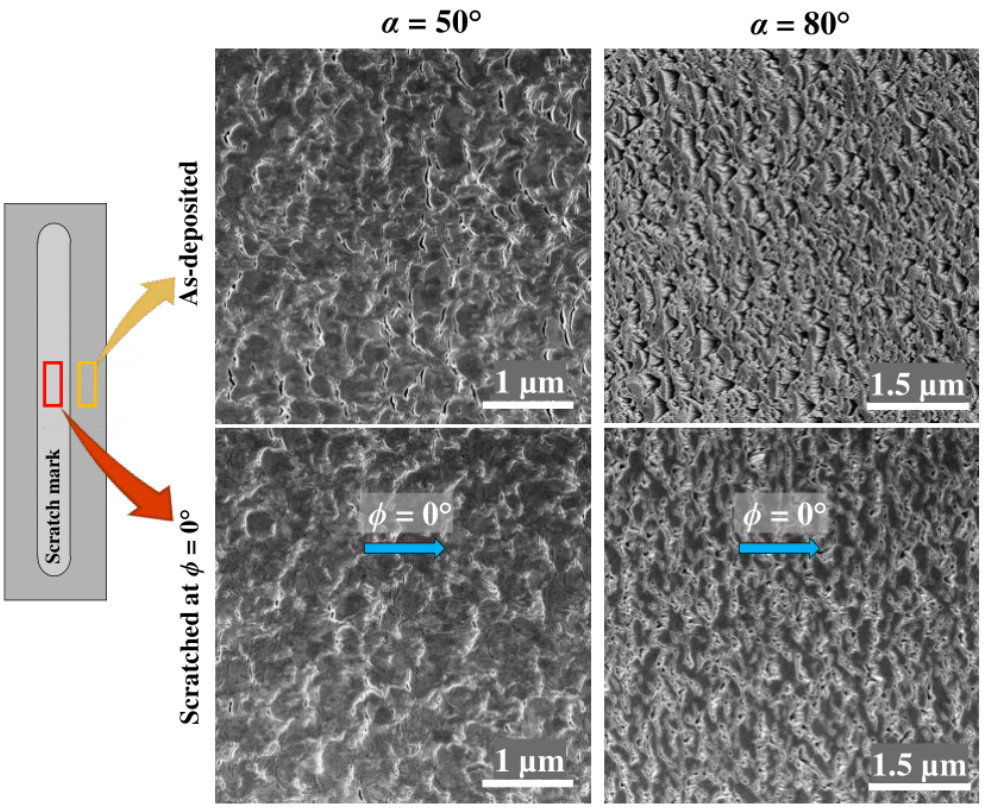

Figure 8: Surface views of a film deposited at $\alpha = 50^\circ$ and 80° in as-deposited and scratched zones. The scratches were performed at $\phi = 0^\circ$, indicated by the blue arrows, and with $F_N = 3.25$ N.

individual column. The columns bend in the direction of their inclination, "lying" on each other, which significantly reduces the volume of voids, and the primarily deformed region is considerably larger than the one observed for $\alpha = 50^\circ$. In both cases, the primarily deformed region predominantly occurs near the surface rather than closer to the substrate.

This difference in the deformation mode for $\alpha = 80^\circ$, as well as the occurrence of deformation in regions farther the substrate, may be attributed to the morphology and porosity of the film. The film deposited at $\alpha = 80^\circ$ is considerably more porous, and the presence of voids leads to more room for plastic deformation of the columns. However, the film density evolves with

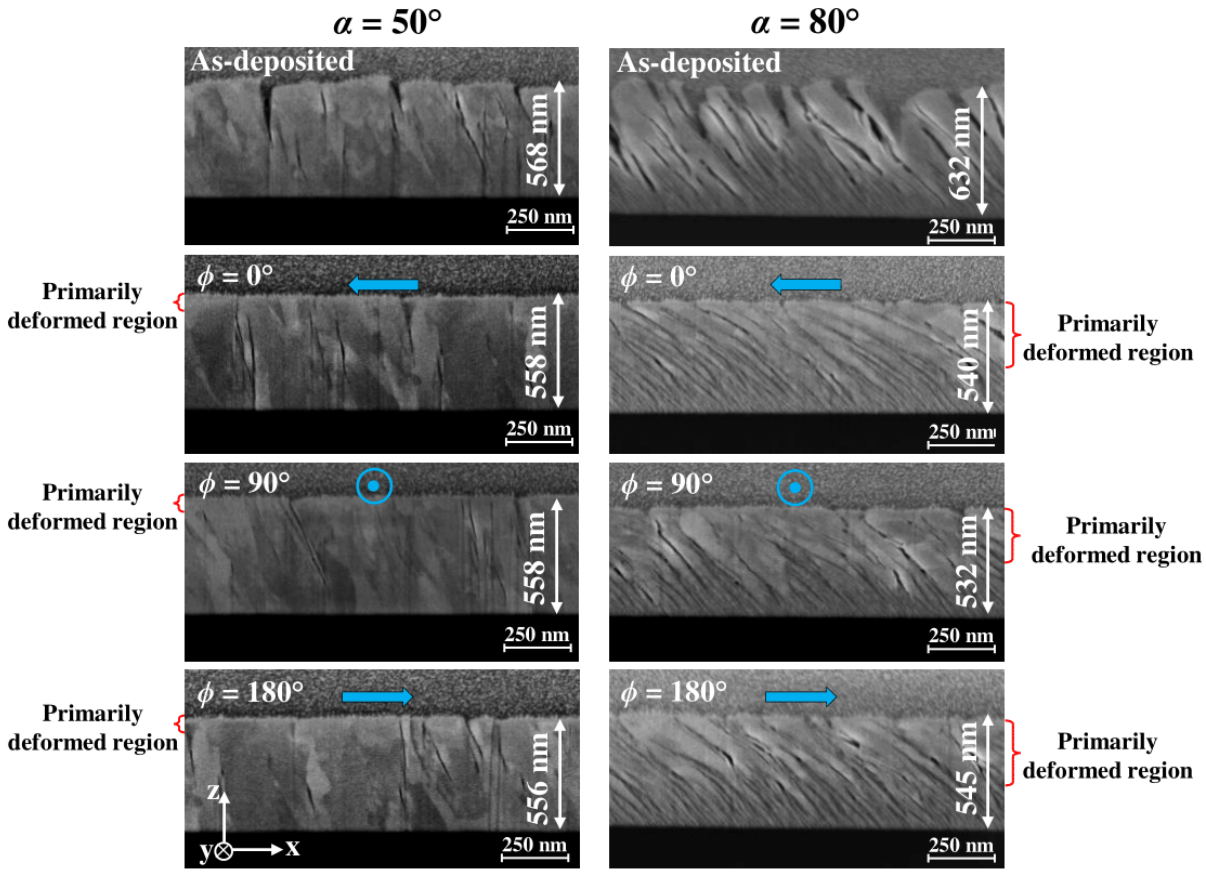

Figure 9: FIB cross-section views of W films deposited at $\alpha = 50^{\circ}$ and 80°, in an as-deposited zone and zones scratched at $\phi = 0^{\circ}$, 90° and 180°. These scratching direction are indicated by the blue arrows.

thickness, i.e., in regions close to the film/substrate interface, there are more small columns and less porosity. This density reduces as the film grows [20].

Concerning the A15-W phase, as previously mentioned, it occurs in the first stages of growing process. Therefore, for the films deposited at $60^{\circ} \leq \alpha \leq 85^{\circ}$, which possess more remaining A15-W after deposition, the regions closer to substrate present more A15-W, while the regions close to the film surface are rich in bcc-W phase. However, A15-W influence on column deformation appears to be negligible. Furthermore, it does not interact with the contact interface during scratch tests.

Comparing the three scratching directions for the film deposited at $\alpha = 80°$, deformation mode seems to be similar between the $\phi = 0°$ and $\phi = 180°$ directions. The columns lean over its neighbor, and as it continues to be loaded, it thins out in xz-plane and increases its width in the y-axis, which can be confirmed by Figure 10.

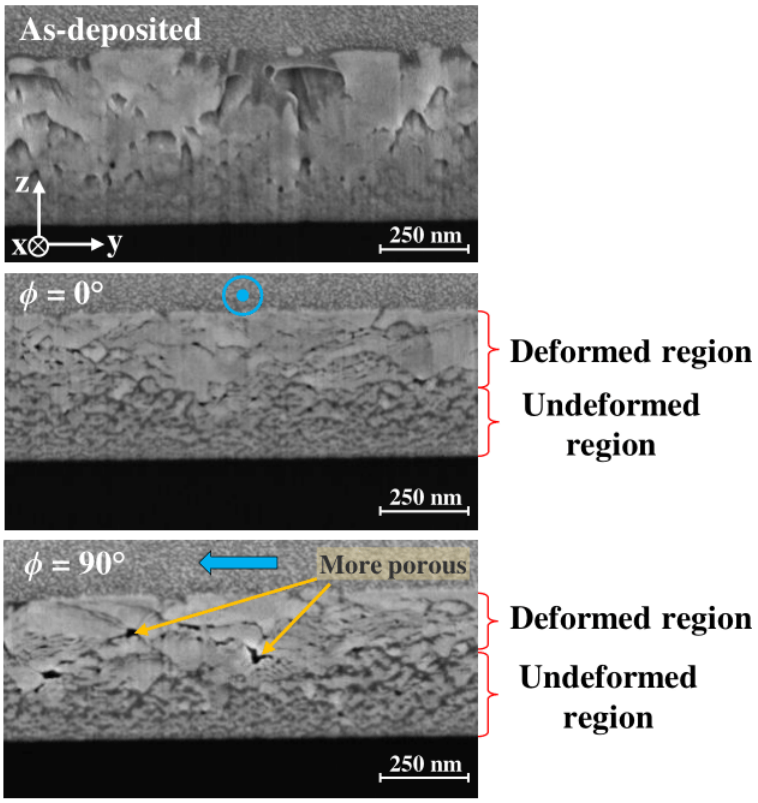

Figure 10: Transversal FIB cross-section views of W films deposited at $\alpha = 80°$, in an as-deposited zone and zones scratched at $\phi = 0°$ and 90°. These scratching direction are indicated by the blue arrows.

On the other hand, when scratching at $\phi = 90°$, the columns, despite deforming in the direction of their inclination, show less deformation in the xz plane, as shown in Fig. 9. It can even be said that the columns present a morphology closer to the as-deposited one. Figure 10 also confirms this by showing different deformation mode on the deformed region. The columns are relatively less deformed in the z axis, the structure is less compact and

columns less flat following the y axis, when compared to $\phi = 0°$.

This difference in the columns deformation mode between the 0°-180° and 90° directions, although subtle, may also be attributed to the morphology. Both shadowing and fanning effects intensify as α increases [66, 20]. The result is the formation of columns chains in the direction perpendicular to the atom flux ($\phi = 90°$). By loading the columns in this direction, the indenter bends them plastically. However, unlike in directions such as 0° and 180° scratching directions, the columns encounter fewer voids and touch their neighbors more quickly, which results in a lower level of deformation, as shown in Figures 9 and 10. The column chains have been already reported for different materials and associated with the anisotropic behavior of some film properties [66, 13, 11, 34].

For the films deposited at $\alpha = 40°$, 50°, and 60°, the friction coefficient (μ) values are consistently higher when scratched in $\phi = 0°$ direction compared to $\phi = 180°$. These films also exhibit a clear morphological transition, progressing from fibrous structures to the early development of pores, and ultimately to low porosity. This indicates that the morphology, along with its associated deformation mechanisms, plays a crucial role in determining both the orthotropic and non-orthotropic friction behavior in these films. However, it appears that an additional factor influences the difference in friction response between the $\phi = 0°$ and $\phi = 180°$ directions.

The combination of the intermediate tilt of these films (β between 13.5° and 24.1°) and their transitional morphologies likely contributes to the non-centrosymmetric anisotropy observed under the scratching conditions applied in this study. While this friction anisotropy is subtle, it aligns with results from previous cited studies [22, 37, 36, 42]. In those works, pronounced non-centrosymmetric anisotropy between 0° and 180° was often reported, particularly for films deposited at α angles greater than 40°, 50°, and 60°.

3.4. Mechanical model

A simple 1D mechanical model is here proposed aiming at helping in understanding the mechanisms associated with the presence or absence of anisotropy in the frictional behavior of the films studied. Contrary to films deposited at $\alpha = 0°$, the observations above prove that sliding on films deposited at higher α values potentially involves two distinct mechanisms:

- Friction, which occurs on top of the columns. It is assumed to be described by an isotropic friction coefficient μ_{iso}.

- Another relative displacement accommodation mechanism, typically plasticity, which is activated when the tangential force applied (T) to the top of the column is equal or higher than a threshold T_S.

In a 1D setting, summarized in Figure 11, friction is allowed to develop along a distance d, whereas the second mechanism is allowed to develop along a distance p,

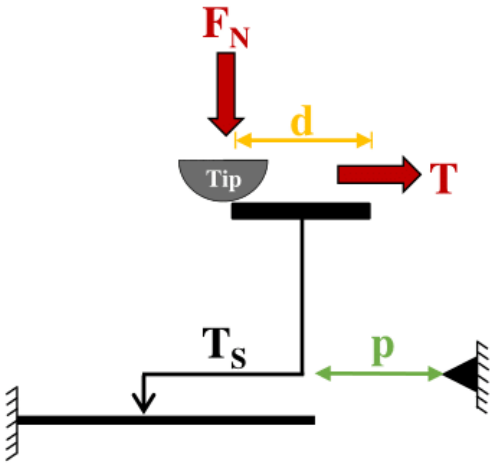

Figure 11: Analytical model where a tip applies a normal load F_N in a column of width d allowing the development of a relative displacement accommodation mechanism. This mechanism is activated when the tangential force $T \geq T_S$, the threshold to activation, and it develops along a distance p.

As a consequence, the energy E_d dissipated when sliding is

$$E_d = T_0 \cdot d + T_S \cdot p = F_N \cdot \mu_{iso} \cdot d + T_S \cdot p \tag{7}$$

At the macroscopic level, this is seen as an apparent friction, for which the dissipated energy is

$$E_d = T_a \cdot (p + d) = F_N \cdot \mu_a \, (p + d) \tag{8}$$

The apparent coefficient of friction thus is

$$\mu_a = \frac{\mu_{iso} \cdot d + \frac{T_S}{F_N} \cdot p}{p + d} \tag{9}$$

The second mechanism is activated only if $T \geq T_S$, so that $\mu_a \leq \mu_{iso}$. When $p \to 0$, $\mu_a \to \mu_{iso}$ and the initial isotropic frictional behavior is recovered. Since p is present a reduction in the apparent friction coefficient μ_a appears. The accommodation mechanism responsible for this reduction may be the plasticity. The model analytically confirms that when $T \geq T_S$ and p increases, the second mechanism reduces μ_a.

As seen from the various observations, more plasticity is developed when sliding at the $\phi = 0°$ and 180° directions, whereas it is inhibited in the $\phi = 90°$ and 270° directions. According to the simple 1D model above, this is consistent with a lower apparent friction coefficient at $\phi = 0°$ and 180° directions compared to $\phi = 90°$ and 270°. This suggests that:

1. The plasticity may be the second accommodation mechanism.
2. The morphology of the film, by limiting its ability to deform plastically in a direction perpendicular to the atom flux, induces the orthotropic frictional behavior reported herein for films deposited at $\alpha \geq 60°$.

In fact, when scratching in the $\phi = 90°$ and 270° directions, the increased column-column contact results in less deformation and greater resistance from the neighboring columns to the indenter's passage. Consequently, it becomes more difficult to continue scratching the film, resulting in higher friction coefficients in these directions. As α increases, more voids and elongated columns accentuate the formation of column chains, thereby enhancing friction anisotropy. A similar approach was explored in the model proposed by [10], where the reaction forces varied depending on the sliding direction and the tilt angle of the surface structures.

Although the simple model effectively illustrates the influence of plastic deformation on friction anisotropy, it does not account for the overall friction coefficient levels of different films. This overall level depends mainly on μ_{iso} of each film, which may vary as the morphological aspect changes.

4. Conclusion

In this study, GLAD tungsten films were sputter-deposited with varying deposition angles ($\alpha = 0°$, 30°, 40°, 50°, 60°, 70°, 80°, and 85°) and deposition times to achieve similar thicknesses. These films were subjected to scratch tests at various directions (defined by the ϕ angle) and normal forces (F_N), allowing a detailed mapping of the frictional behavior. Based on the above research, the following conclusions are summarized.

1. Due to the variation of α, a morphological evolution is observed from dense and fibrous films to well-defined columnar formation with elliptical-shaped structures aligned with the normal direction of atom arrival ($\alpha \geq 60°$). This morphology results from the more pronounced shadowing and fanning effects at higher α values.
2. XRD patterns reveal a predominant bcc-W phase for all films. However, for films deposited at $\alpha \geq 60°$, larger quantities of the A15-W phase are observed. This is also attributed to the higher influence of the shadowing effect during the deposition process, resulting in lower deposition rates and more porous microstructures. These characteristics allow greater interaction between the A15-W phase and residual oxygen, leading to the stabilization of this phase.
3. The friction results show no influence of the normal force during the single scratch tests, which agrees with Coulomb's law.
4. The interpretation of polar plots and the definition of an anisotropy degree parameter, both obtained by a linear model, reveals four distinct groups of films: (i) isotropic ($\alpha = 0°$ and $30°$), (ii) non-centrosymmetrically anisotropic ($\alpha = 40°$ and $50°$), (iii) orthotropic and non-centrosymmetrically anisotropic ($\alpha = 60°$), and (iv) orthotropic ($70° \leq \alpha \leq 85°$). For the orthotropic groups, larger coefficients of friction are obtained for scratches performed at $\phi = 90°$ and $270°$.
5. The orthotropic behavior observed for some films ($60° \leq \alpha \leq 85°$) is attributed to their morphology. The elongated nanostructures form column chains aligned in the normal direction to the atom flux, which coincides with $\phi = 90°$ and $270°$, altering the deformation mode of the columns during scratching. When scratching at $\phi = 90°$, the indenter causes the columns to touch each other more quickly than in other directions, resulting in less deformation of the columns. FIB images reveal that the reduced deformation of the columns is characterized by less bending and wider columns. By allowing plasticity to develop when sliding in the direction of the atom flux while limiting its development in the perpendicular direction, the morphology appears to play a key role in controlling the anisotropic friction behavior. The structural arrangement of the columns influences how the material deforms under different loading directions, which in turn affects the observed frictional responses.

Further work is ongoing to verify if those conclusions apply to other ma-

terials, as well as in mutli-pass friction.

5. Acknowledgments

This work has been achieved in the frame of the EIPHI Graduate school (contract "ANR-17-EURE-0002"). This work is partly supported by the French RENATECH network through its FEMTO-ST technological facility MIMENTO. The support from FEMTO-ST / AMETISTE platform is also acknowledged.

References

[1] Pantelis Sophoclis Alexopoulos and TC O'sullivan. Mechanical properties of thin films. *Annu. Rev. Mater. Sci.*, 20(1):391–420, 1990.

[2] Georg Bauer, Marie-Christin Klein, Stanislav N Gorb, Thomas Speck, Dagmar Voigt, and Friederike Gallenmüller. Always on the bright side: The climbing mechanism of galium aparine. *Proc. R. Soc. London B*, 278(1715):2233–2239, 2011.

[3] FH Baumann, DL Chopp, T Díaz De La Rubia, GH Gilmer, JE Greene, H Huang, S Kodambaka, P O'sullivan, and I Petrov. Multiscale modeling of thin-film deposition: applications to Si device processing. *Mrs Bull.*, 26(3):182–189, 2001.

[4] Bharat Bhushan. *Nanotribology and nanomechanics: An introduction.* Springer, 4th edition, 2017.

[5] Holger F Bohn and Walter Federle. Insect aquaplaning: Nepenthes pitcher plants capture prey with the peristome, a fully wettable water-lubricated anisotropic surface. *Proc. Natl. Acad. Sci.*, 101(39):14138–14143, 2004.

[6] Houssem Boukhalfa, Valérie Potin, and Nicolas Martin. Microstructural analysis and electrical behaviours of co-sputtered W-Ag thin films with a tilted columnar architecture. *J. Phys. D: Appl. Phys.*, 54(25):255304, 2021.

[7] Asma Chargui, Raya El Beainou, Alexis Mosset, Sébastien Euphrasie, Valérie Potin, Pascal Vairac, and Nicolas Martin. Influence of thickness and sputtering pressure on electrical resistivity and elastic wave propagation in oriented columnar tungsten thin films. *Nanomater.*, 10(1):81, 2020.

[8] Asma Chargui, Raya El Beainou, Alexis Mosset, Joseph Gavoille, Pascal Vairac, Sébastien Euphrasie, and Nicolas Martin. Anisotropic thermal conductivity of nanocolumnar W thin films. *Phys. Lett. A*, 426:127878, 2022.

[9] Huawei Chen, Liwen Zhang, Deyuan Zhang, Pengfei Zhang, and Zhiwu Han. Bioinspired surface for surgical graspers based on the strong wet friction of tree frog toe pads. *ACS Appl. Mater. Interf.*, 7(25):13987–13995, 2015.

[10] Qian Cheng, Fan Yang, Han Jiang, and Hongbin Cai. Investigation of the friction reduction and anisotropy of seta structure with large deflection cantilever beam model. *Tribology International*, 172:107640, 2022.

[11] Raya El Beainou, Asma Chargui, Paulo Pedrosa, Alexis Mosset, Sébastien Euphrasie, Pascal Vairac, and Nicolas Martin. Electrical resistivity and elastic wave propagation anisotropy in glancing angle deposited tungsten and gold thin films. *Appl. Surf. Sci.*, 475:606–614, 2019.

[12] Raya El Beainou, Jean-Marc Cote, Vincent Tissot, Valérie Potin, and Nicolas Martin. Resistivity anisotropy of tilted columnar W and WCu thin films. *Surf. Coat. Technol.*, 421:127412, 2021.

[13] Raya El Beainou, Roland Salut, Laurent Robert, Jean-Marc Cote, Valérie Potin, and Nicolas Martin. Anisotropic conductivity enhancement in inclined W-Cu columnar films. *Mater. Lett.*, 232:126–129, 2018.

[14] Y Enomoto and David Tabor. The frictional anisotropy of diamond. *Proc. R. Soc. London A*, 373(1755):405–417, 1981.

[15] Andreas Frisk, Barat Achinuq, David G Newman, Emily Heppell, Maciej Dabrowski, Robert J Hicken, Gerrit van der Laan, and Thorsten Hesjedal. Controlling in-plane magnetic anisotropy of Co films on MgO

substrates using Glancing Angle Deposition. *Phys. Status Sol. (a)*, 220(11):2300010, 2023.

[16] M Gasgnier, L Nevot, P Baillif, and J Bardolle. Characterization and crystalline structures of tungsten thin films. *Phys. Status Solidi (a)*, 79(2):531–542, 1983.

[17] Christoph Gruner, Susann Liedtke, Jens Bauer, Stefan G Mayr, and Bernd Rauschenbach. Morphology of thin films formed by oblique physical vapor deposition. *ACS Appl. Nano Mater.*, 1(3):1370–1376, 2018.

[18] M Halaunbrenner. Directional effects in friction. *Wear*, 3(6):421–425, 1960.

[19] DA Hardwick. The mechanical properties of thin films: A review. *Thin Solid Films*, 154(1-2):109–124, 1987.

[20] Matthew M Hawkeye, Michael T Taschuk, and Michael J Brett. *Glancing angle deposition of thin films: Engineering the nanoscale*. John Wiley & Sons, 1st edition, 2014.

[21] Bo He, Wei Chen, and Q Jane Wang. Surface texture effect on friction of a microtextured poly (dimethylsiloxane)(pdms). *Tribology Letters*, 31:187–197, 2008.

[22] Hiroyuki Hirakata, Taku Nishihira, Akio Yonezu, and Kohji Minoshima. Frictional anisotropy of oblique nanocolumn arrays grown by glancing angle deposition. *Tribol. Lett.*, 44:259–268, 2011.

[23] Motohisa Hirano, Kazumasa Shinjo, Reizo Kaneko, and Yoshitada Murata. Anisotropy of frictional forces in muscovite mica. *Phys. Rev. Lett.*, 67(19):2642, 1991.

[24] Uwe Holzwarth and Hermann Stamm. Mechanical and thermomechanical properties of commercially pure chromium and chromium alloys. *J. Nucl. Mat.*, 300(2-3):161–177, 2002.

[25] Jonathan A Johnson, Tong Su, Eric Chason, and Gregory B Thompson. Inter-relationship of stress and microstructure in BCC and beta-tungsten films. *Surf. Coat. Technol.*, 457:129336, 2023.

[26] Peter H Jost. *Lubrication (Tribology)—A Report of the Present Position and Industry Needs, Department of Education and Science.* London, 1966.

[27] Khedir R Khedir, Ganesh K Kannarpady, Hidetaka Ishihara, Justin Woo, Charles Ryerson, and Alexandru S Biris. Morphology control of tungsten nanorods grown by glancing angle RF magnetron sputtering under variable argon pressure and flow rate. *Phys. Lett. A*, 374(43):4430–4437, 2010.

[28] Tokushi Kizuka, Takehiko Sakamoto, and Nobuo Tanaka. Growth of fine crystals with A-15 type structure in vacuum-deposited tungsten films studied by high-resolution electron microscopy. *J. Cryst. Growth*, 131(3-4):439–447, 1993.

[29] Rahul Krishnan, Michael Riley, Sabrina Lee, and Toh-Ming Lu. Vertically aligned biaxially textured molybdenum thin films. *J. Appl. Phys.*, 110(6), 2011.

[30] George K Larsen, Robert Fitzmorris, Jin Z Zhang, and Yiping Zhao. Structural, optical, and photocatalytic properties of Cr:TiO_2 nanorod array fabricated by oblique angle codeposition. *J. Phys. Chem. C*, 115(34):16892–16903, 2011.

[31] SB Liu, A Peyronnel, QJ Wang, and LM Keer. An extension of the Hertz theory for three-dimensional coated bodies. *Tribology Letters*, 18:303–314, 2005.

[32] Poramate Manoonpong, Dennis Petersen, Alexander Kovalev, Florentin Wörgötter, Stanislav N Gorb, Marlene Spinner, and Lars Heepe. Enhanced locomotion efficiency of a bio-inspired walking robot using contact surfaces with frictional anisotropy. *Sci. Rep.*, 6(1):39455, 2016.

[33] FK Mante, GR Baran, and B Lucas. Nanoindentation studies of titanium single crystals. *Biomaterials*, 20(11):1051–1055, 1999.

[34] Nicolas Martin, Jérémie Sauget, and Tomas Nyberg. Anisotropic electrical resistivity during annealing of oriented columnar titanium films. *Mater. Lett.*, 105:20–23, 2013.

[35] Hamidreza Marvi and David L Hu. Friction enhancement in concertina locomotion of snakes. *J. R. Soc. Interf.*, 9(76):3067–3080, 2012.

[36] Bedabibhas Mohanty, Thomas Alexander Ivanoff, Arif Sinan Alagoz, Tansel Karabacak, and Min Zou. Study of the anisotropic frictional and deformation behavior of surfaces textured with silver nanorods. *Tribol. Int.*, 92:439–445, 2015.

[37] Bedabibhas Mohanty, Beau D Morton, Arif Sinan Alagoz, Tansel Karabacak, and Min Zou. Frictional anisotropy of tilted molybdenum nanorods fabricated by glancing angle deposition. *Tribol. Int.*, 80:216–221, 2014.

[38] JM Nieuwenhuizen and HBi Haanstra. Microfractography of thin films. *Philips Tech. Rev.*, 27(3):87–91, 1966.

[39] M Ohring. *Materials Science of Thin Films*. Academic Press, 2nd edition, 2002.

[40] MJ O'keefe and JT Grant. Phase transformation of sputter deposited tungsten thin films with A-15 structure. *J. Appl. Phys.*, 79(12):9134–9141, 1996.

[41] MJ O'keefe, JT Grant, and JS Solomon. Magnetron sputter deposition of A-15 and BCC crystal structure tungsten thin films. *J. Electron. Mater.*, 24:961–967, 1995.

[42] Meenu Pandey, Divya Verma, Viswanath Balakrishnan, Nitya Nand Gosvami, and JP Singh. Frictional anisotropy of Ag nanocolumnar surfaces. *Tribol. Int.*, 153:106674, 2021.

[43] Paulo Pedrosa, Armando Ferreira, Jean-Marc Cote, Nicolas Martin, Mohammad Arab Pour Yazdi, Alain Billard, Senentxu Lanceros-Mendez, and Filipe Vaz. Influence of the sputtering pressure on the morphological features and electrical resistivity anisotropy of nanostructured titanium films. *Appl. Surf. Sci.*, 420:681–690, 2017.

[44] Paulo Pedrosa, C Lopes, Nicolas Martin, Carlos Fonseca, and F Vaz. Electrical characterization of Ag: TiN thin films produced by glancing angle deposition. *Mater. Lett.*, 115:136–139, 2014.

[45] Valérie Potin, Houssem Boukhalfa, and Nicolas Martin. Oblique angle co-deposition of nanocolumnar tungsten thin films with two W sources: Effect of pressure and target current. *Mater. Chem. Phys.*, 281:125864, 2022.

[46] Ernest Rabinowicz. Direction of the friction force. *Nature*, 179(4569):1073–1073, 1957.

[47] Nikola Radić, Antun Tonejc, Jovica Ivkov, Pavo Dubček, Sigrid Bernstorff, and Zvonko Medunić. Sputter-deposited amorphous-like tungsten. *Surf. Coat. Technol.*, 180:66–70, 2004.

[48] Seyyed Zabihollah Rahchamani, Hamid Rezagholipour Dizaji, and Mohammad Hossien Ehsani. Anisotropic optical properties of ZnS thin films with zigzag structure. *Bull. Mater. Sci.*, 40:897–905, 2017.

[49] Christophe Renault, Kenneth D Harris, Michael J Brett, Véronique Balland, and Benoît Limoges. Time-resolved uv-visible spectroelectrochemistry using transparent 3d-mesoporous nanocrystalline ITO electrodes. *Chem. Commun.*, 47(6):1863–1865, 2011.

[50] David A Rider, Ryan T Tucker, Brian J Worfolk, Kathleen M Krause, Abeed Lalany, Michael J Brett, Jillian M Buriak, and Kenneth D Harris. Indium tin oxide nanopillar electrodes in polymer/fullerene solar cells. *Nanotechnol.*, 22(8):085706, 2011.

[51] K Robbie, LJ Friedrich, SK Dew, T Smy, and MJ Brett. Fabrication of thin films with highly porous microstructures. *Journal of Vacuum Science Technology A: Vacuum, Surfaces, and Films*, 13(3):1032–1035, 1995.

[52] Kevin Robbie and MJ Brett. Sculptured thin films and glancing angle deposition: Growth mechanics and applications. *J. Vac. Sci. Technol. A*, 15(3):1460–1465, 1997.

[53] Stephen M Rossnagel, I Cevdet Noyan, and Cyril Cabral Jr. Phase transformation of thin sputter-deposited tungsten films at room temperature. *J. Vac. Sci. Technol. B*, 20(5):2047–2051, 2002.

[54] Krešimir Salamon, Ognjen Milat, Nikola Radić, Pavo Dubček, Marko Jerčinović, and Sigrid Bernstorff. Structure and morphology of magnetron sputtered W films studied by x-ray methods. *J. Phys. D: Appl. Phys.*, 46(9):095304, 2013.

[55] YG Shen and YW Mai. Influences of oxygen on the formation and stability of A15 β-W thin films. *Mater. Sci. Eng. A*, 284(1-2):176–183, 2000.

[56] Ahcene Siad, Aurélien Besnard, Corinne Nouveau, and Philippe Jacquet. Critical angles in DC magnetron GLAD thin films. *Vacuum*, 131:305–311, 2016.

[57] W Sim, B Kim, B Choi, and J-O Park. Theoretical and experimental studies on the parylene diaphragms for microdevices. *Micro. Tech.*, 11:11–15, 2005.

[58] DO Smith, MS Cohen, and G P+ Weiss. Oblique-incidence anisotropy in evaporated permalloy films. *J. Appl. Phys.*, 31(10):1755–1762, 1960.

[59] Eric So, Melik C Demirel, and Kathryn J Wahl. Mechanical anisotropy of nanostructured parylene films during sliding contact. *J. Phys. D: Appl. Phys.*, 43(4):045403, 2010.

[60] Philippe Stempflé, Aurélien Besnard, Nicolas Martin, Anne Domatti, and Jamal Takadoum. Accurate control of friction with nanosculptured thin coatings: Application to gripping in microscale assembly. *Tribol. Int.*, 59:67–78, 2013.

[61] R Subbiah, S Muthukumaran, and V Raja. Fine-tuning of energy gap, FTIR, photoluminescence and photocatalytic behavior of centella asiatica extract mediated Mn/Mg doped ZnO nanostructure. *J. Mater. Sci.: Materials in Electronics*, 30:17066–17077, 2019.

[62] HL Sun, ZX Song, DG Guo, F Ma, and KW Xu. Microstructure and mechanical properties of nanocrystalline tungsten thin films. *J. Mater. Sci. Tech.*, 26(1):87–92, 2010.

[63] RN Tait, T Smy, and MJ Brett. Modelling and characterization of columnar growth in evaporated films. *Thin Solid Films*, 226(2):196–201, 1993.

[64] Halvor T Tramsen, Stanislav N Gorb, Hao Zhang, Poramate Manoonpong, Zhendong Dai, and Lars Heepe. Inversion of friction anisotropy in a bio-inspired asymmetrically structured surface. *J. R. Soc. Interf.*, 15(138):20170629, 2018.

[65] Mohammad R Vazirisereshk, Kathryn Hasz, Robert W Carpick, and Ashlie Martini. Friction anisotropy of MoS_2: Effect of tip-sample contact quality. *J. Phys. Chem. Lett.*, 11(16):6900–6906, 2020.

[66] D Vick, T Smy, and MJ Brett. Growth behavior of evaporated porous thin films. *J. Mater. Res.*, 17(11):2904–2911, 2002.

[67] FTN Vüllers and Ralph Spolenak. Alpha-vs. beta-W nanocrystalline thin films: A comprehensive study of sputter parameters and resulting materials' properties. *Thin Solid Films*, 577:26–34, 2015.

[68] IA Weerasekera, S Ismat Shah, David V Baxter, and KM Unruh. Structure and stability of sputter deposited beta-tungsten thin films. *Appl. Phys. Lett.*, 64(24):3231–3233, 1994.

[69] S. W. H. Yih and C. T. Wang. *Tungsten-sources, metallurgy properties and application*. New York: Plenum Press, 1979.

[70] Chengjiao Yu and Q Jane Wang. Friction anisotropy with respect to topographic orientation. *Sci. Rep.*, 2(1):988, 2012.

[71] Liping Zhang, Alexandre AS Gonçalves, and Mietek Jaroniec. Identification of preferentially exposed crystal facets by x-ray diffraction. *RSC Adv.*, 10(10):5585–5589, 2020.

[72] Yiping Zhao, Yuping He, and Cameron Brown. Composition dependent nanocolumn tilting angle during the oblique angle co-deposition. *Appl. Phys. Lett.*, 100(3), 2012.

[73] Alfred Zmitrowicz. A theoretical model of anisotropic dry friction. *Wear*, 73(1):9–39, 1981.

[74] Alfred Zmitrowicz. Illustrative examples of centrosymmetric and non-centrosymmetric anisotropic friction. *Int. J. Sol. Struct.*, 29(23):3045–3059, 1992.